Modelling the Flexural Hysteresis Behaviour of Bretelle Dampers based on A Quasi-static Bending Test

Shima Zamanian, Sébastien Langlois, Alex Loignon, Alireza Ture Savadkoohi, M.L.M. François

Modelling the flexural hysteresis behaviour of bretelle dampers based on a quasi-static bending test

Shima Zamanian, Sébastien Langlois, Alex Loignon, Alireza Ture Savadkoohi, Marc L. M. François

Bretelle dampers are made of slack conductor pieces that are used to mitigate aeolian vibration amplitudes. Under cyclic and dynamic excitation, inter-strand friction in slack conductors causes a significant flexural hysteresis leading to the dissipation of high amounts of energies. The objective of this work is to study the flexural hysteresis of three types of slack conductors based on quasi-static bending tests and to reproduce their nonlinear hysteresis behavior using two different approaches; an analytical model using a linear Euler-Bernoulli beam coupled with a Bouc-Wen model, and a finite element model using a superposition of multifiber beam elements with material nonlinearity. The parameters of both models are identified based on the bending test results for different levels of deformation. The developed models in this study can provide a fast tool for manufacturers to identify the dynamical behavior of slack con-ductor and to optimize their damping properties. Furthermore, the bretelle damper model can be integrated into a conductor model in order to study the vibrational behavior of transmission lines equipped with bretelle dampers.

Keywords: Bretelle damper, finite-element analysis, Bouc-Wen, dynamics, hysteresis, transmission lines.

I. Introduction

AEOLIAN vibration causes fretting fatigue at or close to the suspension clamp or to the clamp of dampers where the conductor movement is restrained. Bretelles are used widely in Norway and France to mitigate aeolian vibration amplitude. They are made of slack conductor pieces installed between two spans at the suspension clamp. A slack conductor has a low or negligible axial tension along its length as opposed to a taut conductors. Under bending excitation, friction between the wires of conductors creates a flexural hysteresis. Thus, the moment-curvature relationship is nonlinear; it depends not only on the absolute value of curvature but also on the history of deformation. The hysteresis characteristic contributes to the energy dissipation of conductors. Contrary to taut conductors, slack conductors exhibit significant energy dissipation [1]–[3].

Theoretical models are proposed to predict the nonlinear behavior of conductors with high tension. The model of Papailiou [4] describes the secant bending stiffness as a function of curvature considering the lay angle and friction force between wires. In this model, by increasing the curvature, wires slip layer-by-layer towards the core, and bending stiffness transmits smoothly from maximum bending stiffness EI_{max} (full-stick state) to the minimum bending stiffness EI_{min} (full-slip state). Dastous [5] converted the model of Papailiou based on the tangent bending stiffness method and implemented it in a finite element formulation. Hong et al. [6] improved the model of Papailiou by reconsidering some simplifying assumptions and introducing a new criterion for wire slippage regarding the radial pressure transmission between the layers. The mentioned models were developed for taut conductors (e.g. transmission line conductors), and they do not necessarily apply to slack conductors.

The nonlinearity in the behaviour of the messenger cable of the Stockbridge damper which is the base for power dissipation in the messenger wire of the Stockbridge damper was investigated by Sturm [7] and Diana et al [8]. This nonlinearity was reflected in the nonlinearity of the load-deflection curve of the messenger wire obtained using the flexural rigidity tests. Sauter [3] developed a nonlinear model of a Stockbridge damper. He measured the local moment-curvature of the messenger cable of a Stockbridge damper using a quasi-static test and reproduced the local moment-curvature relationship using Jenkin elements. Foti and Martinelli [9] developed a bilinear elastic-plastic model coupled with the Bouc-Wen model. Langlois and Legeron [10] developed a finite-element model of the messenger cable of a Stockbridge damper with variable bending stiffness by superimposing beam elements with material nonlinearity. The constitutive parameters are identified based on a characterization test. Filliatrault and Stearns [11] performed a quasi-static bending test on low-tension substation conductors. They concluded that low-tension conductors have negligible hysteresis, and their bending stiffness tends toward the minimum bending stiffness.

To study specifically bretelle dampers, field tests have been carried out by Van Dyke et al. [12] and Leblond et al [13]. In their tests, bretelle dampers were installed between two spans at the suspension clamp, and the damping efficiency of the bretelle was measured under wind-induced vibrations. It was shown that in addition to energy dissipation, bretelles transfer part of the vibrational energy to the adjacent span before reaching the suspension clamp. This coupling effect can involve many parameters in the efficiency of bretelle damper. Although bretelles are economically attractive, the optimization of design variables by laboratory tests or field tests is difficult and time-consuming. The flexural behavior of bretelle dampers has not been studied yet. On the other hand, the dynamic model of the bretelle damper with variable bending stiffness has not been developed and validated. This model could be integrated into a model of transmission lines, and the behavior of the system under aeolian vibration could be studied. Moreover, this model allows for optimizing the damping parameters of conductor-damper system.

The first objective of this paper is to study the flexural

TABLE I
PROPERTIES OF CONDUCTOR SAMPLES

Conductor Type	Aster570	Parrot	Curlew
Total area (mm^2)	570	862.4	591.4
Total diameter (mm)	31.05	38.2	31.6
Number of wires (Al/St)	61/0	54/19	54/7
Diameter of steel wires (mm)	-	2.55	3.515
Diameter of aluminum wires (mm)	3.45	4.25	3.515
Lay angle			
-layer 1	7.8	7.2	7.2
-layer 2	10	7.5	10
-layer 3	11	11	11
-layer 4	13	12.8	12.6
-layer 5	-	14.7	-
Linear mass (kg/km)	1574	2879	1979
Global modulus of elasticity (GPa)	54	62.7	69
Maximum bending stiffness (Nm^2)	2184	5089	2392
Minimum bending stiffness (Nm^2)	28.7	67.7	38
Span length (m)	1.242	1.53	1.274
Total length (m)	2	2	2

hysteresis of three types of slack conductors by performing a quasi-static four-point bending test. This test can give a good insight into the bending behavior of bretelles. The next objective is to develop a nonlinear model that predicts the hysteresis behavior of a slack cable under different amplitudes and frequencies. Two models are developed, an analytical model of the slack cable using a linear Euler-Bernoulli beam coupled with a nonlinear Bouc-Wen model [14], [15], and a finite element model by superimposing beam elements with material nonlinearity. The constitutive parameters of the two models are obtained based on the results of the four points bending test.

This paper is structured as follows; Section II presents the methodology of the four-point bending test and the results. Section III presents the development of analytical and finite element model and the parameter identification process, and finally section IV presents the conclusion.

II. FLEXURAL FOUR-POINT EXPERIMENT

The four-point bending test presented in this section aims to obtain the flexural characteristics of the slack conductors. The test procedure and the results of the test are presented in this section.

A. Setup and Procedures

The four-point bending test setup is shown in Fig. 1. The test is performed on three conductor types; Parrot and Curlew which are ACSR conductors (Aluminium Conductors Steel Reinforced) with aluminium alloy 1350-H19 wire, and Aster570 which is AAAC conductor (All Aluminium Alloy conductor) with aluminium alloy 6201-T81 wires. The properties of the conductor specimens are summarized in Table I. Due to the storage process, there was an initial curvature of conductor samples. The setup was adapted for the proper installation of each conductor specimen, considering their initial curvatures.

Four supports at an equal distance of $L/3$ keep the conductor sample in place where L is the span length, which is

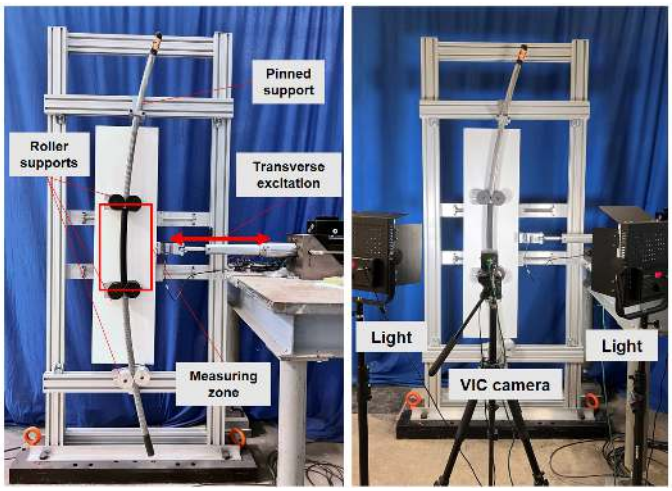

Fig. 1. The four-point bending test setup.

Fig. 2. The VIC method result.

the distance between the two exterior supports (see Table I). This length was defined to obtain a ratio of span length to the diameter of the conductor equal to 40:1 which is within the range recommended for example in ASTM D7264 standard [16] for the application to composite materials. The upper support is a pin connection. The three other supports are made of a pair of low friction rollers that allows rotation and free vertical movement of the conductor. The two central supports are linked to a 5-kN MTS dynamic actuator that applies a sine displacement in the transverse direction. Moment and curvature were measured at the central part of the sample between the two loading supports (measuring zone in Fig. 1), since due to the four-point loading condition, the central part has a constant bending moment and no shear force. To measure the total force applied by the loading supports, a load cell with a capacity of 100 lbs (445 N) is inserted between the piston rod of the actuator and the steel spreader plate. The displacement amplitude was increased successively with pauses between each step, and the test was continued for at least two cycles.

The required level of displacement amplitude reached by each loading support was determined by preliminary tests to ensure that the minimum bending stiffness could be reached at the central part of the conductor. The bending moment at the measuring zone is given by:

$$M = \frac{FL}{3} \tag{1}$$

where F is the force applied by each loading support.

The displacement of the actuator is also recorded, but as it was not possible to obtain a precise evaluation of the curvature from this distant measurement, an image treatment method had to be used. Indeed, the Virtual Image Correlation (VIC) technique [17] is used to assess the silhouette shapes. At each level of displacement, a picture has been taken by a 5 megapixel camera. Each photo was analyzed by the VIC method developed as a MATLAB [18] script. A virtual image (red curves in Fig. 2) based on an arc of a circle was fitted on the border of the image by following the white-to-black gradient of the boundary. The central part of the conductor has been painted black to obtain a good contrast, and a white surface was installed as the background. Two lights have been positioned close to the camera to provide equal illumination and avoid shadows on both sides of the sample. When the best match between the curve and the image was reached, the mean radius of curvature of the inner and outer curve was given. Fig. 2. shows two curves (red lines) that are fitted by the VIC method. The amplitudes of displacement that has been tested are 4 and 10 mm by 0.25 and 1-mm increments with pauses between steps in order to catch images. For each test with a displacement amplitude of 10 mm, a total of 128 photos have been taken and analyzed by the VIC method. To obtain the moment-curvature loops, the initial value of conductor curvature is subtracted from the absolute value of the curvature measured by the VIC method.

B. Effect of Initial Curvature

In this part, the effect of initial curvature on the bending behaviour of the slack conductor has been investigated by measuring the hysteresis cycles for three different initial curvatures, as shown in Fig. 3. The ideal rest state corresponds to a position where the stored elastic energy in the conductor is minimized. To achieve this state, the actuator is utilized to correct the displacement in an iterative manner. The objective is to position the zero force-zero displacement point at the center of the hysteresis loop. At the less curved state and more curved state, by imposing an initial displacement, the natural curvature of the cable is reduced or increased. The results of the test for Aster570 and Parrot for different initial curvatures κ_i are presented in Fig. 4 and Fig. 5. The results show a somewhat larger hysteresis area and slightly lower average slope as a consequence of decreasing the initial curvature. Thus, the change in overall hysteresis and energy dissipation is relatively small when changing the initial curvature.

The tangential bending stiffness EI as a function of relative curvature κ' is calculated and presented in Fig. 6 and Fig. 7. This value is obtained by calculating the slope of the moment-curvature loop starting from the point where the force

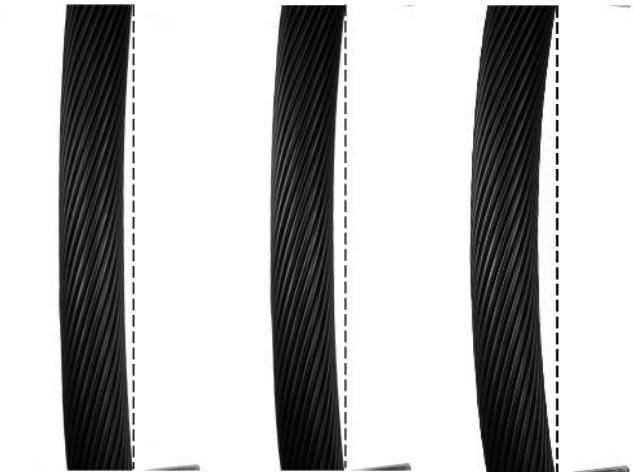

(a) Less curved (b) Ideal rest state (c) More curved

Fig. 3. Initial state of the conductor samples at the onset of the bending test

direction changes from loading to unloading. The slope is measured until it reaches a constant value. In the figures, EI_{max} and EI_{min} represent the maximum and minimum theoretical bending stiffness, respectively, as calculated based on the reference [4]. It can be observed that, in all cases, the initial stiffness of conductors typically begins at approximately 50% of the theoretically calculated EI_{max}. The theoretical assumption behind EI_{max} is that all the wires within the conductor are in a stick condition, behaving like a solid body. However, in practical conductors, there exists some degree of slippage between the wires, which leads to lower values of initial bending stiffness. These findings are in agreement with the research conducted by authors referenced as [19] and [20]. As the curvature increases, there is a point where the bending stiffness reaches approximately EI_{min} and remains relatively constant. This phenomenon occurs due to the slippage of almost all the wires within the conductor.

In addition, the results show that in the more curved state by imposing higher initial curvature (EI at $\kappa' = 0$), the contact area between the wire and therefore the friction forces between the adjacent layers increase. Consequently, at the beginning of the more curved state, the wires remain in the stick state, and the greater number of contact points requires a higher force to overcome the overall friction between the wires. This fact can elevate the sticking stress and leads to higher initial bending stiffness. While the initial EI value is influenced by the initial curvature, it appears that as the curvature is further increased, the bending stiffness exhibits a similar trend regardless of the initial curvature. In other words, the relationship between curvature and bending stiffness becomes relatively consistent, regardless of the specific initial curvature.

C. Effect of Frequency

Conductors usually exhibit a small viscoelastic behavior [3], [10]. To understand the effect of frequency on slack conductors, a continuous sinusoidal displacement has been applied to the system and the force-displacement plot at the loading supports was obtained using the load cell for the

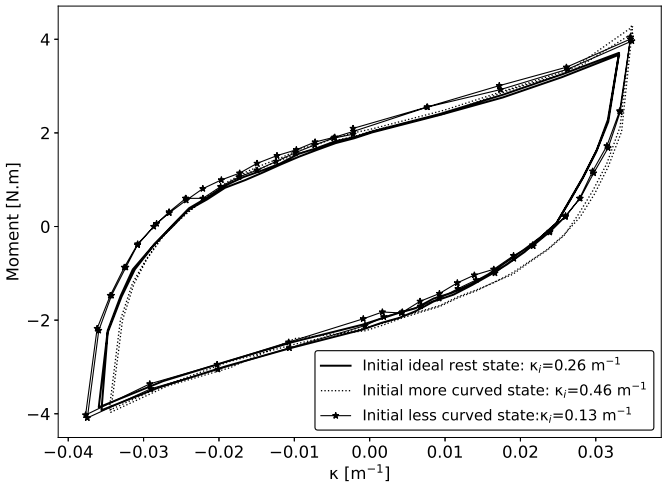

Fig. 4. Moment and curvature relation of AAAC Aster570 at various initial curvatures with a displacement amplitude of 4 mm.

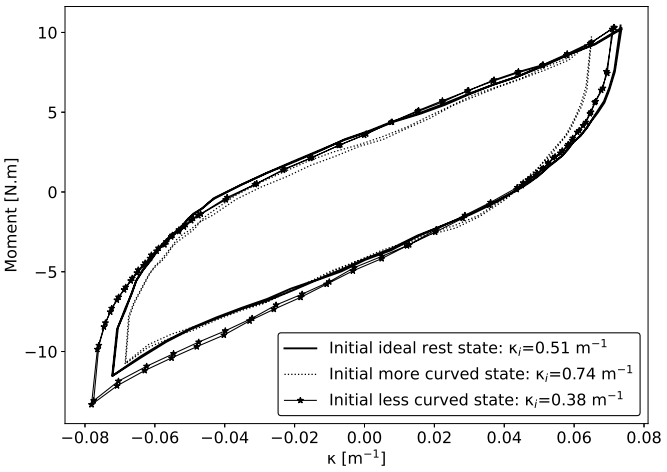

Fig. 5. Moment and curvature relation of ACSR Parrot at various initial curvatures with a displacement amplitude of 10 mm.

amplitudes of 1, 2, 3, 4, 5, 10, 15, 20, 25 mm and the frequencies of 0.3, 0.5, 1 Hz. Tests were performed at higher frequencies but were not used because the inertial forces were difficult to measure and they induced a high level of uncertainties in the evaluation of the forces. The stiffness of the system is determined as the trend line of all points on the hysteresis force-displacement loop. To remove the inertial effects from the system, the new force-displacement hysteresis loop was obtained under the same amplitudes and frequencies after disconnecting the cable. The negative slope observed in the force-displacement loop of the system without the cable reflects the inertial impact of components such as the hydraulic jack, rollers, and other masses involved in the system. This negative slope value is then added to the equivalent stiffness of the system when the cable is connected. Fig. 8 illustrates the equivalent stiffness of the entire system after removing the inertial effects. The variation of the stiffness for all cases is less than 17% and, the flexural behavior of the system is insignificantly affected by the frequency of excitation.

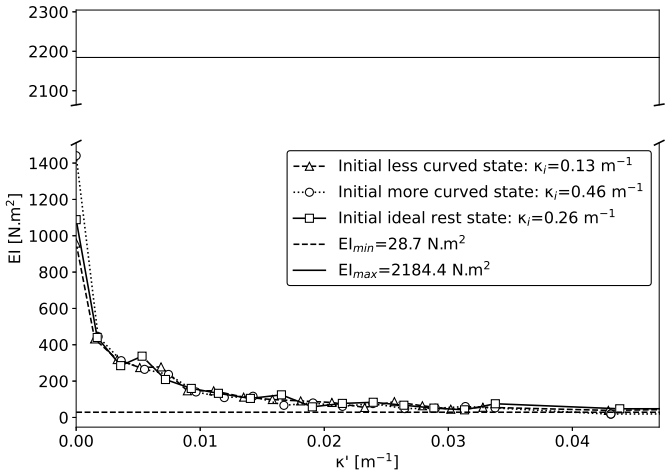

Fig. 6. Tangential bending stiffness as a function of relative curvature for AAAC Aster570 at various initial curvatures.

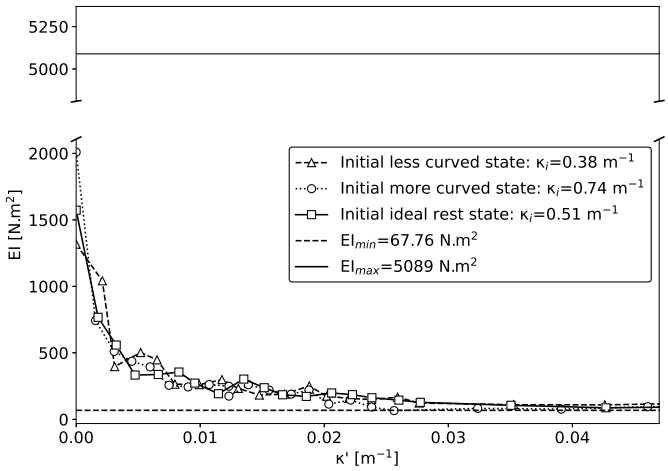

Fig. 7. Tangential bending stiffness as a function of relative curvature for ACSR Parrot at various initial curvatures.

D. Comparative moment and curvature relationship

The experimentally measured moment and curvature relationship of the conductor specimens were obtained at the ideal rest initial state and with the displacement amplitude of 10 mm. The hysteresis cycles of the three types of conductors are shown in Fig. 9. The equivalent stiffness EI_{eq} of all three slack conductors, which is the equivalent slope of the trend line of moment-curvature hysteresis loop, is close to the minimum bending stiffness of the conductor. The ACSR Curlew and AAAC Aster570 have similar geometry (number of layers, diameter of wire, and number of wires), but the Curlew has a steel core. The existence of the steel core results in higher equivalent bending stiffness, and smaller hysteresis area. The ACSR Parrot includes more wires in the layers and the steel core, which results in a larger hysteresis area and equivalent stiffness. In fact, by increasing the number of wires, the contact surface between the wires increases, which results in more friction between the layers.

Comparing to taut conductors [4], [21], the bending stiffness of slack conductors decreases to the EI_{min} value at lower

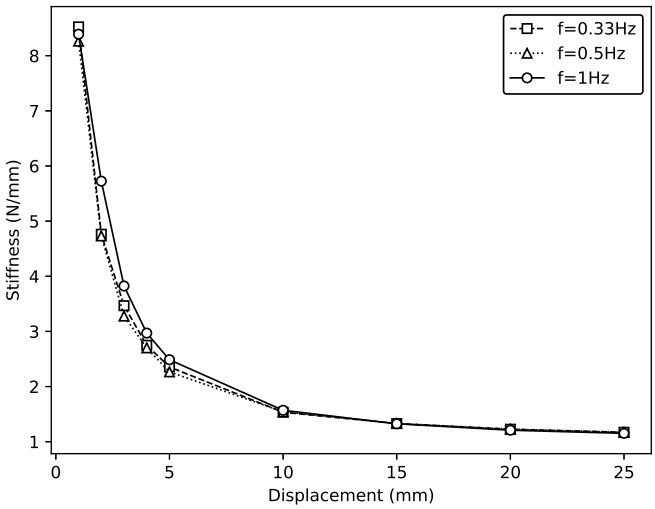

Fig. 8. Relative stiffness versus displacement at various frequencies measured at loading supports for AAAC Aster570.

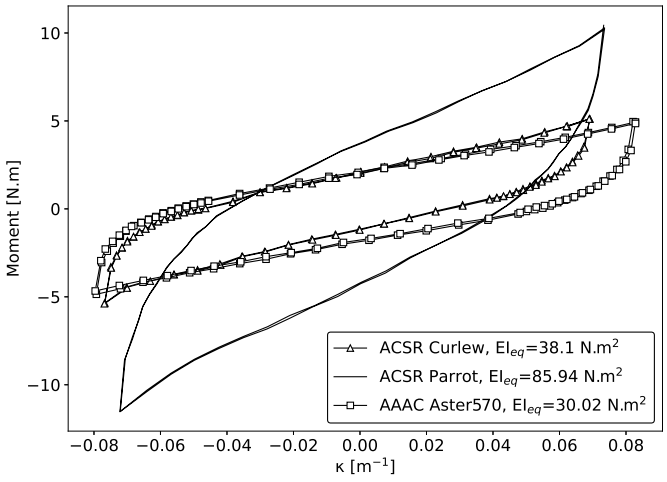

Fig. 9. The measured hysteresis loops of three types of slack conductors with the displacement amplitude of 10 mm.

values of curvature (Fig. 6 and 7). Due to the lack of tension in slack conductors, the normal forces between the layers of the slack conductors are smaller than the taut conductors, and this results in a lower limiting stress. Thus, by increasing the curvature, the wires of the slack conductor shift to the slippage state faster, which leads to lower equivalent stiffness and larger hysteresis area compared to a taut conductor.

III. Modelling Methods

This section presents an analytical and numerical model to describe the bending behaviour of the slack conductors. These models can estimate the nonlinear dynamic behavior and the energy dissipation of slack conductors based on the quasi-static bending properties of the cable. Fig. 10 presents a sketch of the models. It is composed of a simply supported beam with the length of L, which is the span length (see Table I), loaded by two forces at an equal distance at the center of the span. In both models, the initial curvature of the slack conductor is neglected since the results of the tests are obtained based on the relative curvature. In addition, it is assumed that the properties of the conductor are the same along the span. The parameters of both models are identified based on the bending test results of the conductor samples with the ideal rest initial state and presented in the last part of this section.

A. Analytical approach

For describing the bending characteristics of the slack conductor, it is considered as a linear elastic Euler-Bernoulli beam coupled with a Bouc-Wen model [12], [15]. The bending deflection $v(x,t)$ of the linear Euler-Bernoulli beam under an external load $F(t) = \bar{F}\sin(\Omega t)$, see Fig. 10, can be described by the following equation [22]:

$$EI(\frac{\partial^4 v(x,t)}{\partial x^4}) + F(t)\delta(x - L/3) + F(t)\delta(x - 2L/3) = m\frac{\partial^2 v(x,t)}{\partial t^2} + c\frac{\partial v(x,t)}{\partial t} \quad (2)$$

where δ is Dirac delta function, EI is the bending stiffness, $\bar{F}$ is the force amplitude, Ω is the excitation frequency, m is the mass per unit length and c is the viscous damping.

The boundary conditions at the external supports are:

$$\begin{aligned} v(0,t) &= 0, \forall t \\ v(L,t) &= 0, \forall t \\ v''(0,t) &= 0, \forall t \\ v''(L,t) &= 0, \forall t \end{aligned} \quad (3)$$

where the prime denotes the derivative with respect to the space variable x. In every mode, the system exhibits a consistent vibrational pattern, resulting in the division of the displacement function into distinct time and space components. The displacement function v(x,t) can be represented in the following manner:

$$v(x,t) = \Gamma(x)g(t) \quad (4)$$

where $\Gamma(x)$ is the natural mode shape of the system and $g(t)$ is the corresponding generalized coordinate. By substituting Eq. (4) into Eq. (2) and solving the eigenvalue problem related to the free response of the system, and incorporating the boundary conditions described in Eq. (3), the modal characteristics of the system, including the natural modes and corresponding frequencies can be determined as follows:

$$\Gamma_i(x) = A_i \sin(\beta_i x) \quad (5)$$

$$\omega_i = \beta_i^2 \sqrt{\frac{m}{EI}} \quad (6)$$

where $i = 1, 2, 3, ...$ denotes the mode number. The variable $\beta_i = i\pi/L$ is calculated using the characteristic equation ($sin(\beta L) = 0$). The coefficients A_i can be obtained from mass normalization of modes as follows:

$$\int_0^L m\Gamma_i(x)^2 dx = 1 \quad (7)$$

Based on the deflection shape of the conductor specimen in the bending test, the system is projected on its first mass

normalized mode. Thus, the response of the system Eq. (4) can be rewritten as:

$$v(x,t) = \Gamma_1(x) g_1(t) \tag{8}$$

By substituiting Eq. (8) in Eq. (2), applying the boundary conditions Eq. (3), the equation of motion in the modal coordinate after addition of nonlinear Bouc-Wen model could be expressed as [23], [24]:

$$\ddot{g_1}(t) + 2\xi\omega_1\dot{g_1}(t) + \alpha\omega_1^2 g_1(t) + (1-\alpha)\omega_1^2 z(t) = f(t) \tag{9}$$

$$\dot{z}(t) = \dot{g_1}(t)[1 - \mid \frac{z(t)}{g_y} \mid^n (\beta + \lambda sgn(z\dot{g_1}))] \tag{10}$$

where the dots denotes the derivative with respect to time, sgn is the sign function, $\xi = c/2m\omega_1$ is the proportional damping, ω_1 is the first natural circular frequency and $f(t) = (\Gamma_1(L/3) + \Gamma_1(2L/3))\bar{F}\sin(\Omega t)$ is the modal force.

The Bouc-Wen model is linked to the equation of the beam as a superposition of a linear elastic force $\alpha\omega_1^2 g_1(t)$ and a hysteretic force $(1-\alpha)\omega_1^2 z(t)$. The hysteretic force involves the hysteretic internal variable $z(t)$ which is governed by the nonlinear first-order differential Eq. (10). The Bouc-Wen model parameters, β, γ are non-dimensional parameters that control the shape and size of the hysteresis loop, α is the post-yielding to pre-yielding stiffness ratio, g_y is the generalized yield displacement and n is a positive number that controls the smoothness of the transition from the elastic to the inelastic region.

The response of the system is calculated by direct integration of Eq. (9) and Eq. (10) using the "ode45" function in MATLAB [18]. To be able to use this function, Eq. (9) and Eq. (10) have to be transformed into a system of first-order equations as below:

$$\begin{aligned} \dot{Y}(1) &= Y(2) \\ \dot{Y}(2) &= -2\xi\omega_1 Y(2) - \alpha\omega_1^2 Y(1) - (1-\alpha)\omega_1^2 Y(3) + f(t) \\ \dot{Y}(3) &= Y(2)[1 - \mid \frac{Y(3)}{g_y} \mid^n (\beta + \lambda sgn(Y(3)Y(2)))] \end{aligned} \tag{11}$$

where $Y(1) = g_1(t)$, $Y(2) = \dot{g_1}(t)$ and $Y(3) = z(t)$.

The following initial conditions are considered for this system:

$$t = 0 \rightarrow \begin{cases} Y(1) = 0, & \dot{Y}(1) = 0 \\ Y(2) = 0, & \dot{Y}(2) = 0 \end{cases} \tag{12}$$

After obtaining the response of the system numerically, the total restoring force $F_r(t)$ is expressed as:

$$F_r(t) = \alpha\omega_1^2 g_1(t) + (1-\alpha)\omega_1^2 z(t) \tag{13}$$

thus, the moment $M(t)$ at the central part of the beam between the loads is calculated as:

$$M = F_r(t)L/6 \tag{14}$$

The curvature is calculated using the second derivative of Eq. (8) as follows:

$$\phi(x,t) = \frac{\partial^2 \Gamma_1(x)}{\partial x^2} g(t) \tag{15}$$

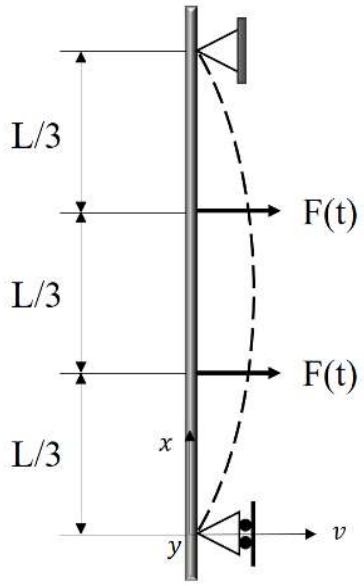

Fig. 10. Sketch of the four-point bending test.

To reproduce the results of the bending test, the Bouc-Wen parameters need to be identified for each conductor sample such that the moment-curvature relationship corresponds to the bending test. In this model, the excitation force amplitude $\bar{F}$ for each conductor type is equal to the maximum force measured experimentally to reach the 10 mm displacement at the loading supports. To accurately characterize the bending behaviour of the slack conductors, a very low excitation frequency Ω of 0.3 Hz has been considered to excite the first mode of the system which is compatible with the deflection shape of the conductor specimen in the bending test. The frequency of excitation is considered to be constant and equal for all samples. To help the convergence of the response the proportional damping ξ of 0.5% and the time step of 0.001 s is considered.

B. Numerical Approach

To develop the numerical model, the open-source finite element software code-aster 2018 [25] was implemented. This model is developed to predict the nonlinear response of the slack conductor, thus a direct transient analysis with the time step of 0.001 s is used.

To model the hysteretic behaviour of the slack conductor, nonlinear Euler-Bernoulli beam elements with material and geometrical nonlinearities are superimposed with an elastic Euler-Bernoulli beam. The mesh size is equal to 80 mm. For each conductor layer, one nonlinear beam is considered on the nodes. The nonlinear beams have elastic-perfectly-plastic behaviour; the elastic regime represents the sticking state of each layer of conductor, which occurs when the curvature is not high enough to dominate the friction forces between the wires. The moment in sticking state M_i^{stick} is a linear function of curvature with a constant slope that represents the stick stiffness EI_i^{stick} of each layer and can be calculated as [5]:

$$M_i^{stick} = EI_i^{stick}\kappa \qquad i = 1, 2, 3, 4, ..., n \tag{16}$$

where n is the number of layers and κ is curvature. In the perfectly plastic regime, the moment is constant and equal to the yield moment of each nonlinear beam corresponding to the maximum moment reached before the onset of slippage of each conductor layer. The yield moment and the bending stiffness of each nonlinear beam determine the curvature criterion for entering the perfectly-plastic regime.

As mentioned earlier, one linear elastic beam is also considered on the nodes which represents the slipping state of layers that occurs when the friction forces cannot prevent the relative movement between the wires. The internal moment of the elastic beam M_{min} is a linear function of curvature with a constant slope that is equal to the minimum bending stiffness of the conductor [5]:

$$M_{min} = EI_{min}\kappa \tag{17}$$

EI_{min} is the minimum bending stiffness, which is due to the bending of all wires around their neutral axis. These elements are superimposed at each mesh subdivision and have the same group of nodes. Thus, at each node, all beam elements experience the same deflection, and the properties of each beam contribute to the total stiffness matrix. Thus, the total moment is equal to [5]:

$$M = \begin{cases} M_{min} + \sum_i M_i^{stick} & \kappa \leqslant \kappa_{slip} \\ M_{min} + \sum_i M_i^{y} & \kappa > \kappa_{slip} \end{cases} \tag{18}$$

In code-aster, multi-fiber beam (MFB) elements are able to model the behaviour of structures with material nonlinearities under static and dynamic loading. Thus, each layer of the conductor is modeled with an MFB element. The elastic limit of each MFB can be controlled by defining the yield stress. It can be calculated from the yield moment M_i^y and the moment of inertia of each beam I_i using the following equation:

$$\sigma_i = M_i^y h_i / I_i \qquad i = 1, 2, 3, 4, ..., n \tag{19}$$

where h_i is the distance of the fibers of each beam compared to the central axis of the section and can be given by:

$$h_i = \sqrt{\frac{I_i}{A_i}} \qquad i = 1, 2, 3, 4, ..., n \tag{20}$$

where I_i is the moment of inertia of each beam and $A_i = A/n$ is the total area of the conductor cross-section A, divided by the number of layers n. According to Eq. (13), (14), and (15), by adjusting the sticking stiffness EI_i^{stick} and yield moment M_i^y of each beam, the overall moment-curvature hysteresis loop of the conductor samples can be reproduced based on the results of the four-point bending test. In this model, the excitation force has a displacement amplitude of 10 mm and a frequency of 0.3 Hz. The moment and curvature at the central part of the span were calculated directly by the code-aster model.

TABLE II
THE PARAMETERS OF THE BOUC-WEN MODEL

Conductor Type	Aster570	Parrot
EI (Nm^2)	387.55	1290
α	0.11	0.125
g_y	0.1	0.075
n	1	1
β	20	18
γ	85	18

TABLE III
THE PARAMETERS OF THE NUMERICAL MODEL

Conductor Type	Aster570	Parrot
EI_i^{stick} (Nm^2)		
i=1	31.91	73.38
i=2	13.5	9.79
i=3	30.29	12.99
i=4	96.39	130.8
i=5	837.01	300.26
i=6	-	740.78
M_i^y (N.m)		
i=1	-	-
i=2	0.3	0.2
i=3	0.12	0.21
i=4	0.18	0.63
i=5	0.58	0.48
i=6	-	0.5

C. Parameter Identification

The constitutive parameters of the models are identified based on an average of the experimentally measured moment-curvature loops of the samples of each conductor type for the bending test with the ideal rest initial state. For each conductor type, the constitutive parameters of the models should be determined. In this study, the parameters of Aster570 and Parrot are identified and validated.

According to Eq. (5), (6) and (9), the Bouc-Wen parameters; α, g_y, n, β, γ and the bending stiffness of the Euler-Bernoulli beam EI need to be obtained in order to reproduce the right moment-curvature relation. EI controls the slope of the hysteresis loop in the elastic region and it can be estimated directly from the experimental moment-curvature loop. The Bouc-Wen parameters were identified iteratively by trial and error to reach the best match between the analytical and experimental results. Table II presents the sets of parameters that are identified for each conductor sample.

According to Eq. (13), (14), and (15), the parameters of the numerical model that contribute to controlling the global flexural behaviour of the model are EI_i^{stick} and M_i^y of each beam. These parameters were determined with an iterative process and can define the state of each layer (sticking/slipping). Based on the initial bending stiffness of the conductors that have been calculated from the tests (Fig. 6 and 7), the initial guess for EI_i^{stick} of each beam is:

$$EI_i^{stick} = (EI_i^{max} - EI_i^{min})/2 \tag{21}$$

where EI_i^{max} and EI_i^{min} are the maximum and minimum bending stiffness of each layer that have been calculated theoretically based on [4]. The identified parameters for the numerical model are presented in table III.

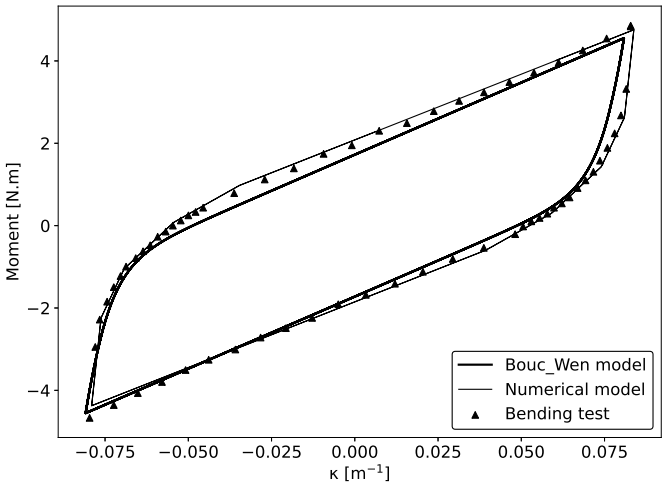

Fig. 11. Characterization of AAAC Aster570 conductor.

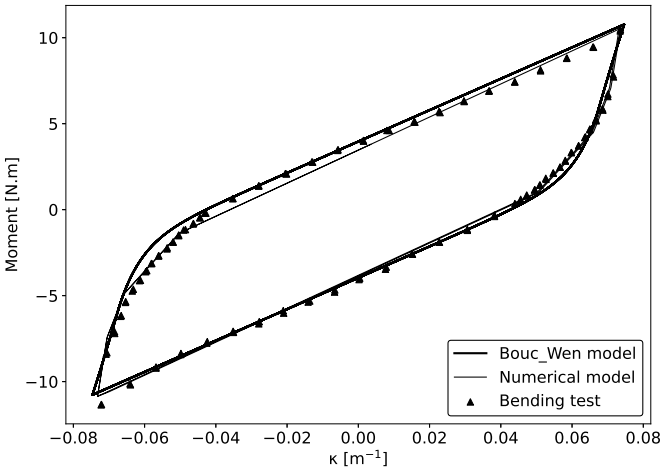

Fig. 12. Characterization of ACSR Parrot conductor.

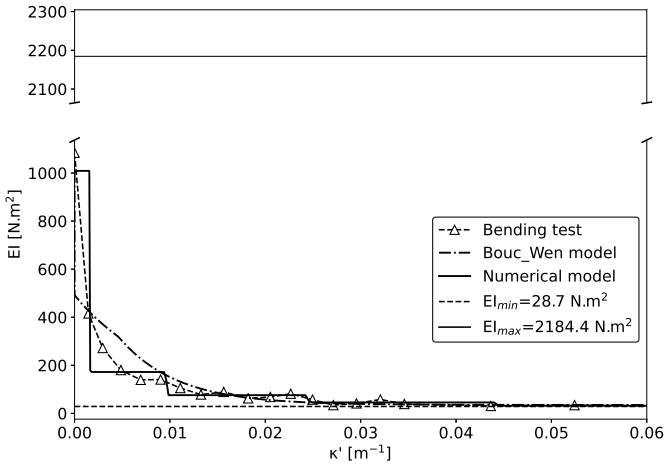

Fig. 13. The tangential bending stiffness as a function of curvature for Aster570 conductor, comparison between the models with the experimental results

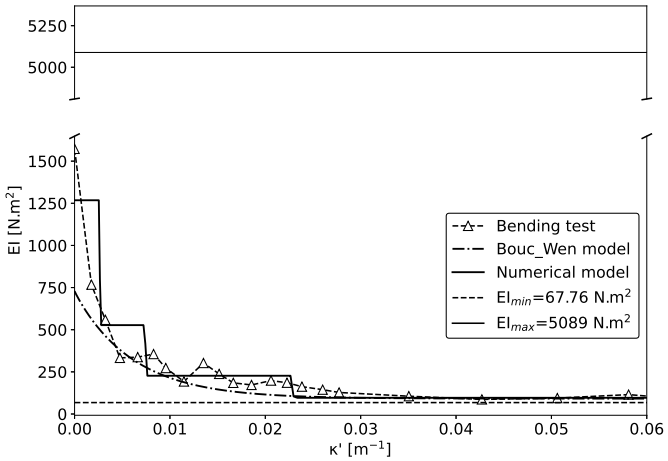

Fig. 14. The tangential bending stiffness as a function of curvature for Parrot conductor, comparison between the models with the experimental results

In Fig. 11 and 12 numerically and analytically obtained hysteresis cycles are compared to those measured experimentally. Both models can reproduce the real flexural behaviour of the slack conductors with good precision. Using the moment-curvature relation, the tangential bending stiffness as a function of the curvature is calculated and compared in Fig. 13 and 14. The finite element model corresponds better to the experimental results in comparison to the Bouc-Wen model. In fact, in the finite element model by considering the same number of MFB as the number of conductor layers and controlling the parameters of each beam, the gradual slippage of the wires can be modeled, which results in a more accurate bending behaviour.

IV. Conclusion

The deformation of the bretelle dampers, which is a slack conductor piece, during the Aeolian vibration is mainly due to bending. Thus, to study the flexural behaviour of bretelle dampers, a quasi-static four-point bending test has been performed on three different slack conductors. The measured moment-curvature relation indicates the existence of significant hysteretic behaviour in slack conductor originating from the friction between the wires, which leads to the energy dissipation characteristics of the slack conductors. Calculation of the tangential bending stiffness from the measured moment and curvature relationship showed that the bending stiffness of the slack conductors starts from lower values than EI_{max} and drops quickly to EI_{min} at low curvatures and stays constant by further increasing the curvature. The equivalent bending stiffness of the slack cable tends toward the EI_{min}.

The flexural behaviour of the slack cable was reproduced by two different nonlinear models; a Bouc-Wen model and a finite element model. The constitutive parameters of the models are identified based on the experimentally obtained data in the time domain. Both models use a direct time integration method, which allows the calculation of dynamical problems. It should be noted that to use the models, the properties of a conductor need to be characterized. The finite element model allows the inclusion of the bretelle damper into a conductor model for vibration analysis or the optimization of the bretelle

damper configuration. However, the Bouc-Wen model and its integration into the conductor model would need further analytical development. Furthermore, some additional tests on conductors are suggested for instance to study the effect of span length on the bending stiffness and also to extend the models to other geometries of conductors and try to get a generalized behaviour of slack conductors in bending.

ACKNOWLEDGMENT

The authors would like to express their gratitude to RTE (Réseau de Transport d'Électricité), INNOVÉÉ, and NSERC (Natural Sciences and Engineering Research Council of Canada) for their generous funding and support towards this research project. Special thanks are also extended to Hydro Quebec, RTE, and Statnett for providing the necessary specimens to conduct the experimental tests.

REFERENCES

[1] J. Chan, D. Havard, C. Rawlins, G. Diana, L. Cloutier, J.-L. Lilien, C. Hardy, J. Wang, and A. Goel, "Epri transmission line reference book: wind-induced conductor motion." *EPRI, N° 1018554*, 2009.

[2] J. Lemaitre, J.-L. Chaboche, A. Benallal, and R. Desmorat, *Mécanique des matériaux solides-3e éd.* Dunod, 2020.

[3] D. Sauter, "Modeling the dynamic characteristics of slack wire cables in stockbridge dampers. dr.-ing," Ph.D. dissertation, Dissertation, Department of Applied Mechanics, Darmstadt University of ..., 2003.

[4] K. Papailiou, "On the bending stiffness of transmission line conductors," *IEEE Transactions on Power Delivery*, vol. 12, no. 4, pp. 1576–1588, 1997.

[5] J.-B. Dastous, "Nonlinear finite-element analysis of stranded conductors with variable bending stiffness using the tangent stiffness method," *IEEE Transactions on Power Delivery*, vol. 20, no. 1, pp. 328–338, 2005.

[6] K.-J. Hong, A. Der Kiureghian, and J. L. Sackman, "Bending behavior of helically wrapped cables," *Journal of engineering mechanics*, vol. 131, no. 5, pp. 500–511, 2005.

[7] R. G. Sturm, "Vibration of cables and dampers: Part ii," *IEEE Transactions on Power Apparatus and Systems*, vol. Trans. Am. Inst. Electr. Eng, no. 55(6), pp. 673–688, 1936.

[8] R. Claren and G. Diana, "Mathematical analysis of transmission line vibration," *IEEE Transactions on Power Apparatus and Systems*, vol. PAS-88, no. 12, pp. 1741–1771, 1969.

[9] F. Foti and L. Martinelli, "Hysteretic behaviour of stockbridge dampers: modelling and parameter identification," *Mathematical Problems in Engineering*, vol. 2018, 2018.

[10] S. Langlois and F. Legeron, "Prediction of aeolian vibration on transmission-line conductors using a nonlinear time history model—part i: Damper model," *IEEE transactions on power delivery*, vol. 29, no. 3, pp. 1168–1175, 2013.

[11] A. Filiatrault and C. Stearns, "Flexural properties of flexible conductors interconnecting electrical substation equipment," *Journal of Structural Engineering*, vol. 131, no. 1, pp. 151–159, 2005.

[12] P. Van Dyke, C. Hardy, M. St-Louis, and J.-L. Gardes, "Comparative field tests of various practices for the control of wind-induced conductor motion," *IEEE transactions on power delivery*, vol. 12, no. 2, pp. 1029–1034, 1997.

[13] A. Leblond, P. Van Dyke, L.-P. Bibeau, and C. Hardy, "Test line assessment of mechanical power flow in overhead conductors and efficiency of damping devices," in *ASME International Mechanical Engineering Congress and Exposition*, vol. 26751. American Society of Mechanical Engineers, 1997, pp. 169–176.

[14] R. Bouc, "Forced vibrations of mechanical systems with hysteresis," in *Proc. of the Fourth Conference on Nonlinear Oscillations, Prague, 1967*, 1967.

[15] Y. Wen, "Equivalent linearization for hysteretic systems under random excitation," 1980.

[16] "Standard Test Method for Flexural Properties of Polymer Matrix Composite Materials," ASTM International, PA 19428-2959. United States, Standard, 2021.

[17] M. L. M. François, "Uncertainty of the virtual image correlation method," *International Journal for Numerical Methods in Engineering*, vol. 123, no. 18, pp. 4367–4390, 2022.

[18] MATLAB, *9.7.0.1190202 (R2019b)*. Natick, Massachusetts: The MathWorks Inc., 2018.

[19] F. Lévesque, S. Goudreau, S. Langlois, and F. Légeron, "Experimental study of dynamic bending stiffness of acsr overhead conductors," *IEEE Transactions on Power Delivery*, vol. 30, no. 5, pp. 2252–2259, 2015.

[20] C. SC22-WG01, "Report on aeolian vibration," *Electra, no. 124, pp. 41–77,*, 1986.

[21] J.-P. H. Paradis and F. Légeron, "Modelling of the free bending behavior of a multilayer cable taking into account the tangential compliance of contact interfaces," in *Ninth International Symposium on Cable Dynamics*, 2011, pp. 18–20.

[22] L. Meirovitch, *Fundamentals of vibrations*. Waveland Press, 2010.

[23] A. Ture Savadkoohi and C.-H. Lamarque, "Dynamics of coupled dahl type and nonsmooth systems at different scales of time," *International Journal of Bifurcation and Chaos*, vol. 23, no. 07, p. 1350114, 2013.

[24] F. Ikhouane and J. Rodellar, *Systems with hysteresis: analysis, identification and control using the Bouc-Wen model*. John Wiley & Sons, 2007.

[25] E. de France, "Finite element $code\_aster$, analysis of structures and thermomechanics for studies and research, year = 1989–2018," Open source on www.code-aster.org.